Journal of
Nanoscience and Nanotechnology
Vol. 6, 1–15, 2006

REVIEW

Advances in Contemporary Nanosphere Lithographic Techniques

Xiaoyu Zhang, Alyson V. Whitney, Jing Zhao, Erin M. Hicks, and Richard P. Van Duyne*

Department of Chemistry, Northwestern University, 2145 Sheridan Road, Evanston, IL 60208, USA

Nanosphere lithography (NSL) is an inexpensive, high throughput, materials general nanofabrication technique capable of producing a large variety of nanoscale structures including well-ordered 2 dimensional nanoparticle arrays. In this review, we will summarize the most recent advances in the fabrication of size-tunable nanoparticles using NSL. Four examples of new NSL-derived materials will be described: (1) The development of a method to release NSL nanoparticles from the substrate for applications in solution environments, (2) the fabrication of triangular nanoholes with reactive ion etching, (3) the electrochemical fine tuning of the structure of a silver nanoparticle and the wavelength of its localized surface plasmon resonance (LSPR), and (4) the growth of ultra thin protective dielectric layers on NSL-fabricated Ag nanotriangles using atomic layer deposition (ALD).

Keywords: Nanosphere Lithography, Reactive Ion Etching, Atomic Layer Deposition, Localized Surface Plasmon Resonance, Nanowell, Silver, Indium Tin Oxide.

CONTENTS

1. INTRODUCTION

The research of nanomaterials and their size-dependent properties is driven by the demand for ever smaller device features needed to achieve improved performance and decreased cost in the microelectronics, communications, and data storage industries. Developments in nanotechnology rely on the design and fabrication of nanostructures with features in the 1–100 nm size regime. Arrays of nanoparticles and nanopores in the sub-100 nm size regime are widely used in applications such as catalysis,[1] sensing,[2,3] optics,[4] molecular separation,[5,6] molecular reaction dynamics,[7] single molecule detection,[8] and electronics.[9] Consequently, there is an increasing demand for rapid, massively parallel fabrication strategies for these nanostructures. The ideal nanofabrication technique would be materials and substrate general, inexpensive, tunable in nanoparticle size, shape, and spacing parameters, and massively parallel.

Recent advances in both wet chemical and lithographic techniques have made it possible to synthesize a wide range of particle sizes and geometries.[10,11] The wet chemical syntheses can produce nanosized colloids in many different shapes. The most commonly prepared shapes are spheroids,[12] triangular prisms,[13,14] rods,[15,16] and cubes,[17] which are produced by the reduction of a metal salt. In addition, large aspect ratio (ratio of length to width) nanoparticles can be synthesized by the electrochemical reduction of metal salts in the presence of a surfactant or template.[18–21] Recently, Murphy and co-workers reviewed the chemical synthesis of one-dimensional nanostructures of gold and silver via surfactant-directed routes.[22] The aspect ratios of the resultant nanostructures can be easily varied over a wide range (up to 23) by adjusting the experimental parameters. Wiley and co-workers discuss a different approach, based on polyol reduction, to the large-scale synthesis of silver nanostructures with a variety of well-defined shapes, such as cubes, wires, quasi-spheres, or triangular plates.[11,23] The colloids have been widely used in both biolabelling and biosensing, since they can be dispersed throughout the object of study, such as cells[24] and tissue samples.[25]

*Author to whom correspondence should be addressed.

Xiaoyu Zhang is a graduate student in Van Duyne lab at Northwestern University. She received her B.S. degree in materials chemistry from Peking University in 2001 and will be a postdoctoral fellow at the University of Illinois, Urbana Champion in 2006. Her research interests include nanoscience, plasmonic materials, surface-enhanced spectroscopy, microbiology, and electrochemistry.

Alyson V. Whitney is a doctoral candidate in chemistry at Northwestern University. She received her undergraduate degree in chemistry from the University of California in Santa Barbara in 2001. She then traveled to Australia to conduct research with Dr. Paul Mulvaney at the University of Melbourne in Australia. Currently Alyson is a 4th year graduate student in Richard P. Van Duyne's laboratory where her research focuses on applying surface-enhanced Raman spectroscopy to a wide range of applications including art conservation and catalysis.

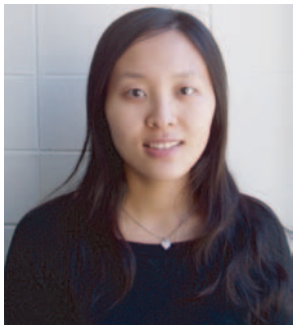

Jing Zhao is a doctoral candidate in chemistry at Northwestern University. She received her undergraduate degree in chemical physics from the University of Science and Technology of China in 2003. Currently Jing is a 3rd year graduate student joint between Richard P. Van Duyne's and George C. Schatz's groups. Her research focuses on experimental and theoretical studies of the mechanisms and applications of localized surface plasmon resonance and surface-enhanced Raman spectroscopy.

Erin McLellan Hicks is a graduate of Rensselaer Polytechnic Institute, magna cum laude with a B.S. in chemistry with a minor in materials science and engineering. While at RPI she did a variety of research from organometallic synthesis and characterization to microelectronics fabrication. She is currently working as a joint member of Professors Richard P. Van Duyne and Kenneth G. Spears in the Department of Chemistry at Northwestern University, focusing on nanoparticle fabrication and optics.

Richard P. Van Duyne is Charles E. and Emma H. Morrison Professor of Chemistry at Northwestern University. He is the discoverer of surface-enhanced Raman spectroscopy (SERS), inventor of nanosphere lithography (NSL), and developed ultrasensitive nanosensors based on localized surface plasmon resonance (LSPR) spectroscopy. His research interests include surface-enhanced spectroscopy, nanofabrication, nanoparticle optics, combined scanning probe microscopy/Raman microscopy, Raman spectroscopy of mass-selected clusters, ultrahigh vacuum surface science, structure and function of biomolecules on surfaces, and surface-enhanced spectroscopic methods for chemical and biological sensing.

The nanoparticle synthesis methods discussed above create suspensions of nanoparticles in solution. Another class of techniques addresses substrate-bound nanostructure fabrication. The standard lithographic techniques used to fabricate such nanostructures with controlled size, shape, and spacing include photolithography,[26] electron beam lithography (EBL),[27] and focused ion beam lithography (FIB).[5] Photolithography is widely used because it is massively parallel; however, its resolution is currently limited by diffraction to ∼100 nm.[26] EBL and FIB are capable of producing arbitrarily shaped nanoparticles and nanopores with extremely high resolution (e.g., 2 and 6 nm for EBL[28] and FIB,[29] respectively). In EBL, the desired pattern is serially produced by exposing a thin layer of photo-resist (e.g. poly(methyl methacrylate)) to high energy electrons, followed by chemical development and deposition of the noble metal. The interaction of electrons with the photo-resist causes local changes to the polymer chains, making the material soluble in a developing solution. However, the high cost and serial nature of EBL and FIB present serious challenges to their high volume manufacture. Consequently, much recent research has been focused on the development of alternative parallel lithographic methods.

An alternative method for the large-scale production of surface-bound nanoparticle arrays is nanosphere lithography (NSL), which is now being employed in laboratories around the world as an inexpensive, inherently parallel, high-throughput, and materials general nanofabrication technique.[30–32] NSL has also been demonstrated to be well-suited to the synthesis of size-tunable noble metal nanoparticles in the 20–1000 nm range. The conventional NSL process begins with self-assembly of a nanosphere mask onto a substrate, followed by deposition of a material(s) through the mask. Computer simulations using a spring-block stick-slip model have been done to reveal the dynamics leading to pattern formation after a colloidal suspension of nanospheres drying on a frictional substrate.[33] The nanosphere diameters determine the size and interspacing distance of the NSL produced nanoparticles. The nanosphere used as deposition masks are usually polystyrene or silicon, available in a variety of sizes (100–2000 nm).[34] Recently, modified polystyrene, such as poly-(diallyldimethylammonium chloride)/poly(sodium 4-styrenesulfonate) thin shell, has been utilized to fabricate NSL template.[35, 36]

The supporting substrates underneath nanospheres can be glass,[37, 38] mica,[37, 39] silica,[37, 40] copper,[41, 42] and indium tin oxide.[43, 44] In general, the substrate to be patterned is positioned normal to the direction of material deposition. The resultant nanoparticles have an inplane shape and interparticle spacing determined by the projection of the nanosphere mask interstices onto the substrate. A monolayer mask produces nanoparticles having a triangular inplane shape arranged on the surface with P_{6mm} symmetry. The ratio of the interparticle spacing to the in-plane perpendicular bisector is a fixed value, ca. 2.5 (Ref. [45]). Angle-resolved nanosphere lithography (AR NSL), a simple variant on conventional NSL, produces vastly different and increasingly flexible nanostructures by controlling the angle between the surface normal of the sample assembly and the propagation vector of the material deposition beam.[46] The nanosphere mask registry also affects the resultant nanostructure. The range of accessible structural motifs can be further expanded by performing a series of material depositions on the same sample under AR NSL conditions.[4] Another similar fabrication method, namely, shadow nanosphere lithography, makes morphologies such as cups, rods, and wires by rotating the tilted nanosphere masks during deposition.[47, 48]

Nanosphere lithography is a materials-general nanofabrication technique. A variety of materials, such as noble metal,[30, 43] magnetic materials,[49] semiconductor materials,[50, 51] polymers,[52–54] and protein[55] can be used as deposition materials in NSL. The magnetic nanostructures are currently the subject of much interest due to their enormous potential applications in high density storage. Periodic magnetic nanoparticle arrays have been successfully produced using the electrodeposition[56, 57] or electron beam evaporation of nickel and cobalt.[49] On NSL-fabricated nickel nanoparticles, well-aligned carbon nanotubes were grown in a hot filament plasma-enhanced chemical vapor deposition system. Furthermore, the carbon nanotube site density and diameter can be easily controlled by the size of the polystyrene nanospheres.[1, 58] For example, isolated carbon nanotubes can be fabricated by using relatively large polystyrene spheres (∼1–2 μm in diameter).[59] An alternative fabrication of carbon nanostructures based on NSL is to infiltrate sucrose solution, a carbon precursor, into the voids between a nanosphere mask. Carbonization of sucrose ended up with the formation of glassy carbons.[50]

Recently, NSL has been explored to fabricate metal oxide catalyst nanostructures. At present, conventional methods, such as salt precipitation, calcinations, and solid phase reactions, are the most widely used processes for fabrication of the metal oxide catalysts. The particles produced by solution methodologies, however, tend to agglomerate, are nonuniform in size and shape, and are not amenable to surface characterization by experimental techniques such as electron spectroscopy or scanning probe microscopy. To overcome those disadvantages, Lenzmann and coworkers initiated the fabrication of uniform and well ordered metal oxide nanoparticles (Y_2O_3) using NSL.[60] Bullen and coworkers have been able to directly grow TiO_2 nanoparticles on NSL masks by back-filling the vacuum chamber with O_2 during the evaporation of Ti. They also demonstrated that NSL is quite general and should be applicable to growing many oxide nanoparticles on a variety of substrates including single crystals.[51]

Nanoporous polymer structures can be obtained by using NSL, sintering rheology and selective dissolution.[52–54] These polymer nanowells showed the ability to

capture negatively-charged gold nanoparticles or DNA-capped gold nanoparticles.[53] These polymers nanostructures, analogous to the size of cells, have been of great interest in micro- and nano-devices for *in vivo* applications. Lu and coworkers has presented a review on the fabrication techniques of biodegradable polymer nanostructures.[61]

The combination of NSL and oxygen plasma[62, 63] or other reactive ion etching (RIE)[40] greatly broadens the scope of NSL to include strategies for the fabrication of several new nanoparticle structural motifs. Laser[64] and oxygen plasma[62, 63, 65] are able to induce the size decrease of self assembled silicone and polystyrene nanospheres. Therefore, nanohole arrays can be fabricated with an extra step of oxygen plasma prior to metal deposition. By incrementing the etch time, the diameter of the nanospheres is steadily reduced, resulting in samples with metallic nanoparticles of increasing size until they eventually merge to form hole arrays.[63, 66] The NSL produced nanowells can be used as deposition template to fabricate silicon,[65, 67, 68] noble metal,[69] cobalt,[56, 57] and gallium nitride nanorod arrays.[70] On the other hand, with the application of NSL and RIE, our previous work has demonstrated the fabrication of ordered arrays of in-plane, triangular cross-section nanowells with in-plane widths ranging from 44 to 404 nm and depths ranging from 25 to 250 nm.[40] These substrates are useful as templates for the growth of other nanomaterials. For example, Zheng and co-workers have demonstrated selective growth of GaAs quantum dots in the uniform and periodic arrays of triangular Si nanowells.[71]

NSL enables a fabrication of defect-free Ag nanoparticle arrays with areas of 10–100 μm^2 (Fig. 1) that are large enough to permit microprobe studies of nanoparticle optical properties. In our group, we focus on the fabrication of noble metal nanoparticles by NSL and explore the optical properties, especially, surface plasmons of these nanoparticles. Surface plasmons come in two basic forms, propagating and localized. In a flat smooth film, the surface plasmon polaritons (SPPs) are propagating evanescent electromagnetic waves at the metal-dielectric interface as a result of collective oscillations of the conduction electrons in the metal.[72] Localized surface plasmon resonances (LSPRs) are observed in isolated nanoparticle systems.[73] These optical modes lead to enhanced electromagnetic fields outside the particle surfaces, which are important in the interaction of the particles with their external environment.[37, 74, 75] NSL has been utilized to fabricate highly uniform arrays of noble metal nanoparticles with LSPR extinction wavelength maxima (λ_{max}) that can be tuned by changing the size, shape, and composition of the nanoparticle.[76] The classical electromagnetic approach available for modeling the optical properties of metal nanoparticles is Mie theory, an exact solution to Maxwell's equations for the scattering of light by a spherical particle.[77, 78] Mie theory is limited to spherical particles. Provided that the particles are large enough so that

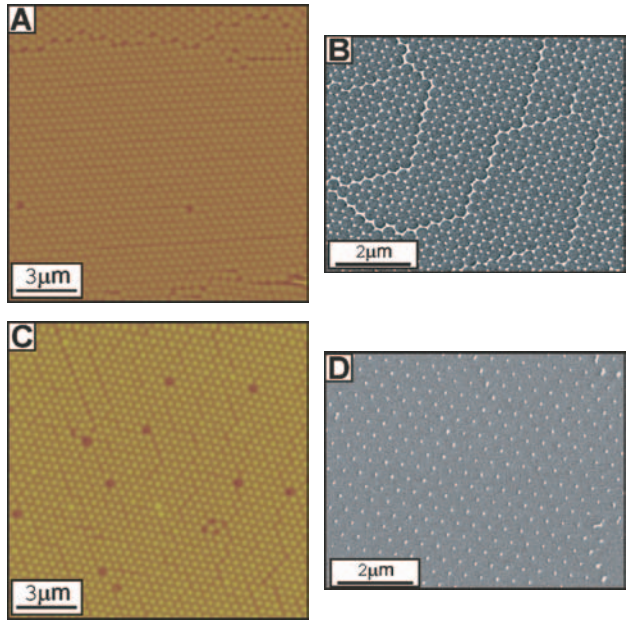

Fig. 1. Comparison of AFM images of $D = 400$ nm nanospheres deposited onto a glass substrate with SEM images of the periodic particle arrays. (A) and (C) correspond to tapping mode AFM images of bare nanosphere samples. (B) and (D) correspond to SEM images of the samples after deposition of 50 nm Ag followed by nanosphere removal. Reproduced with permission from [90], A. D. Ormonde et al., *Langmuir* 20, 6927 (**2004**). © 2004, American Chemical Society.

classical electromagnetic theory applies, Mie theory can be applied to describe particles of any size. Computationally speaking, when the sphere sizes are close to visible wavelengths, the calculations become increasingly intensive.[79] For asymmetric nanoparticles—or even spherical nanoparticles in an asymmetric environment—we turn to numerical methods for solving Maxwell's equations, including discrete dipole approximation (DDA),[73, 80, 81] multiple multipole (MMP),[82] finite difference time domain (FDTD),[83] and T-matrix methods.[84] In the DDA method, the particle of interest, which can be of any arbitrary shape, is divided into a polarizable cubic array. The induced dipole polarizations in these cubes are determined self-consistently. Then, properties such as the extinction cross section are determined in terms of the induced polarizations. The time-consuming part of the calculation involves evaluating dipole fields at each cube due to polarization in the other cubes. Then these fields can be evaluated using Fourier methods.[85]

Two notable consequences of LSPR excitation are

(1) selective photon absorption and scattering allowing for the monitoring of the LSPR with ultraviolet-visible (UV-vis) spectroscopy and

(2) a locally enhanced electromagnetic field permitting optical detection of adsorbates with high sensitivity.[2, 45, 75]

With an extreme sensitivity to dielectric environment, these nanoparticles are well suited as optical nanosensors

and have been successfully applied in a diverse range of fields including biological[2, 39, 86–89] and chemical sensing.[3]

In this review, we will summarize our recent efforts to broaden the scope of NSL to include strategies for the fabrication and characterization of several new nanoparticle structural motifs. The remainder of this review will be organized into five parts.

(1) We will discuss the development of a method based on the convective self-assembly (CSA) of the nanospheres, which improves the drop-coating methods by decreasing the defect percentage within two-dimensional arrays.[90]

(2) We will illustrate a novel method to produce solution-phase triangular silver nanoparticles, which are prepared by nanosphere lithography and are subsequently released into solution.[91]

(3) We will introduce a fabrication method of ordered arrays of in-plane, triangular cross-section nanowells based on the combination of NSL and RIE.[40]

(4) We will highlight an electrochemical approach to quantitatively modify the geometry of NSL produced Ag nanotriangles on an indium tin oxide (ITO) electrode surface.[43] And

(5) we will utilize ultra thin Al_2O_3 produced by atomic layer deposition (ALD) to probe both the long and short range distance dependence of the LSPR effect on Ag nanoparticles.[92]

1.1. Fabrication of Large Areas of Well-Packed Monolayers by Convective Self Assembly and Scanning UV-Visible Spectroscopy

We developed a method based on CSA of the nanospheres which improves upon the drop-coating methods by decreasing the defect percentage within two dimensional arrays. With this technique it is possible to produce well packed samples over a 1 cm^2 area. The experimental set-up is depicted in Figure 2. The formation of a monolayer array is controlled by three processes:

(1) capillary forces,

(2) convective transfer of the nanospheres from the bulk of solution to the thin wetting film, and

(3) water evaporation.[93]

A pressure differential is created when the solution drop is placed along the edge of the spreader. This causes a capillary effect which transfers some of the solution from the bulk drop to the dry zone forming a thin wetting film. (Expanded view in Fig. 2) When the evaporation begins, the nanospheres preferentially form a hexagonally close packed monolayer. To maintain this process the stage is moved in the opposite direction to the monolayer formation at a constant velocity. The optimal velocity was found to be 0.035 mm/sec to form a closely packed monolayer over a large section of the substrate. It is essential that the withdrawal rate is equivalent to the evaporation rate of the liquid in the dry zone in order to form a monolayer of nanospheres. If the rate is too slow, the nanospheres will accumulate and multilayers of nanospheres will dominate the substrate surface. Conversely, if the rate is too fast, it will produce amorphous adsorption with multiple empty zones. In addition to the control of rate, the distance between the spreader and the substrate, h, also has an effect on the formation process of nanosphere monolayer. The control of h allows for a regulation over the amount of bulk solution and the density of nanospheres in the solution that migrate from the wet zone to the dry zone. The addition of a thin Teflon membrane equalizes the capillary forces across the sample which eliminates the requirement for extreme precision in the lateral placement of the spreader. Besides, the high flexibility of the Teflon membrane prevents it from disrupting the formation of monolayers. Nitrogen was flowed in a direction perpendicular to the line of template formation to stimulate the evaporation of the nanosphere suspension.

One of the most prevalent methods to evaluate the template quality produced by CSA is AFM imaging. However, there are several severe limitations to this approach, such as restricted access to sample sites and unacceptable time (on the order of hours) required to resolve images from the large area of a sample. Alternatively, an optical method of evaluation would eliminate these restrictions while allowing for quantitative evaluation of the samples. Ideally one would be able to monitor the optical properties of the bare nanospheres themselves. The spectra of two-dimensional arrays, however, are very difficult to interpret due to diffuse scattering produced by defects in the packing arrangement of the colloidal template. Therefore, the nanosphere template was used to create well-ordered arrays of silver nanotriangles. The optical properties of silver nanoparticle arrays have been well documented and provide a good starting point to test the performance of CSA. Utilization of the sensitivity of the LSPR is an excellent way to assess the

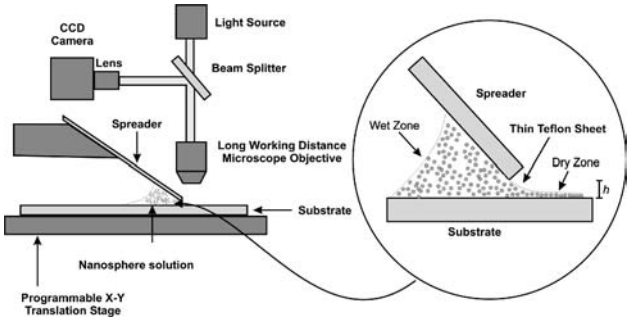

Fig. 2. Shown is a schematic of the convective self-assembly apparatus. The expanded view shows the meniscus formation when the spreader is located at a position h above the substrate as well as the dry and wet zones critical to colloidal crystal formation. Reproduced with permission from [90], A. D. Ormonde et al., *Langmuir* 20, 6927 **(2004)**. © 2004, American Chemical Society.

quality and morphology of the nanosphere packing. Well ordered CSA templates produce highly uniform nanoparticle arrays with characteristic spectra, while poorly packed nanosphere templates do not. This difference can be used to characterize the quality of each template produced.

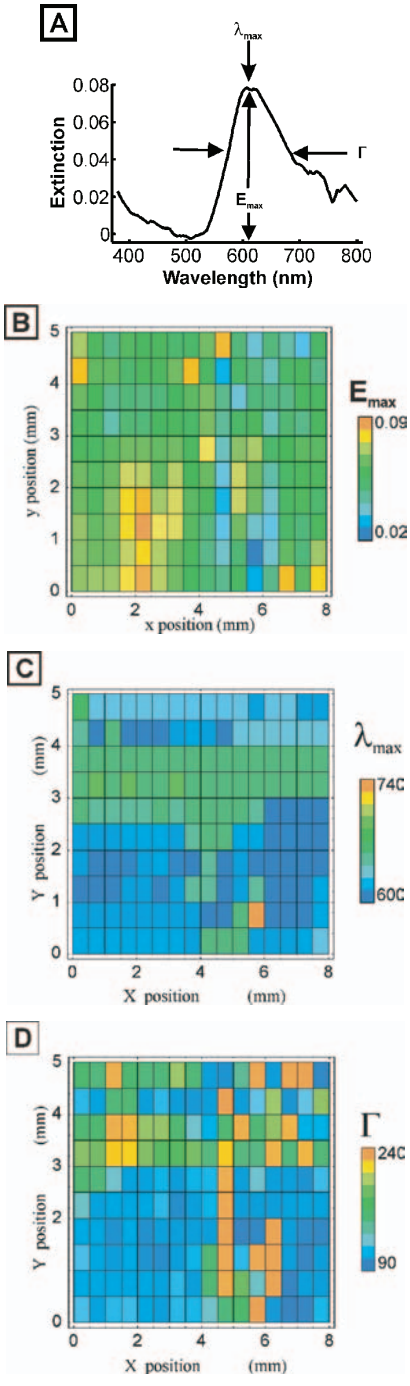

Fig. 3. Shown are the UV-vis extinction spectroscopy and image maps of Ag nanoparticle arrays formed from nanospheres with $D = 400$ nm. 3A shows a representative single spectrum from the sample. Image maps: 3B corresponds to E_{max}, 3C to λ_{max}, and 3D to Γ. Reproduced with permission from [90], A. D. Ormonde et al., *Langmuir* 20, 6927 **(2004)**. © 2004, American Chemical Society.

The properties of nanoparticle arrays formed by a template of nanospheres with the diameter (D) of 400 nm have been well studied and documented, providing necessary information for the evaluation of the quality of CSA produced nanosphere templates. The LSPR spectra of silver nanoparticle arrays ($d_m = 50$ nm) prepared using this template ($D = 400$ nm) is known to have a extinction maximum peak wavelength (λ_{max}) at about 600 nm with ~0.1 absorbance units in magnitude (E_{max}) and 100 nm full width half maximum (Γ).[85] Defects in the nanosphere mask and insufficient or overabundant quantities of nanospheres result in defects in the metal nanoparticle array, which cause perturbations in the LSPR spectra. Samples with a large shift in λ_{max} or extremely wide LSPR band width are often associated with large silver islands. A separate data file was created for each of the three important characteristics of the spectra. A single spectrum from the sample, shown in Figure 3A, confirmed that the sample exhibited the characteristic extinction peak for the template used. This extinction spectrum is an averaging of the many different plasmon resonances across the sample. With the use of scanning UV-visible spectroscopy, gray scale images (Figs. 3B–D) were generated of E_{max}, λ_{max}, and Γ, respectively, to monitor the plasmon resonance in

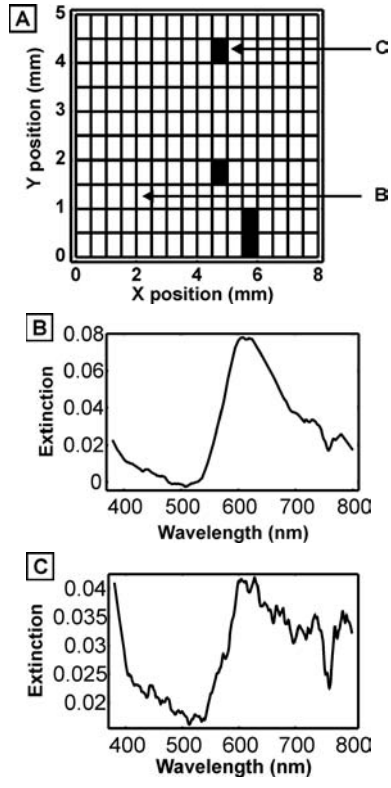

Fig. 4. Shown are the UV-vis extinction spectroscopy and image map of Ag nanoparticle arrays. 4A shows a spatial plot of the data with restrictions applied for E_{max}, λ_{max}, and Γ. Spectra: 4B corresponds to a good pixel on the sample while 4C corresponds to a pixel which falls below the minimum requirements to be considered acceptable as a good quality peak. Reproduced with permission from [90], A. D. Ormonde et al., *Langmuir* 20, 6927 **(2004)**. © 2004, American Chemical Society.

smaller areas. In looking at these smaller areas, variations can be seen in each map. While each individual peak characteristic is important, all three must be considered together when assessing the actual sample quality. An acceptable peak is defined as:

(1) Large E_{max} representing high signal to noise ratio,

(2) reproducibility of λ_{max} ($\pm$20 nm for measurements in ambient conditions), and

(3) Γ of 50 to 150 nm to eliminate noise peaks as well as those found in large absorption bands (as in the case of a silver island).

In the summation spectra shown in Figure 4 the white areas indicate locations of acceptable peaks while the black areas represent pixels outside of the applied restrictions. This summation spectra allows for the determination of high quality samples for the use in additional studies and, additionally, it directs the experimenter to the sections of a sample that are of the best quality which are most likely to produce high quality results in future spectroscopic analyses.

2. SOLUTION-PHASE AG NANOTRIANGLES FABRICATED BY NSL

Traditionally, noble metal nanoparticles are synthesized in solution phase by reducing a metal salt in a controlled environment.[94] While in this work, we present an alternative to synthesize precisely-controlled solution-phase nanoparticles from NSL fabricated nanoparticles confined on glass.[91] In previous studies, the nanoparticle adhesion to glass is found to be less than 10 nN (normal force) is required for delamination.[88] This property allows for the intentional removal of the nanoparticles from the glass substrates. Because NSL is a powerful tool to fabricate monodisperse nanoparticles with well-defined shape and size,[30, 95] the methods developed in this work can be used to produce nanoparticles with controllable geometry in solution phase.

Ag nanoparticles were fabricated by NSL using nanospheres with diameter, $D = 400$ nm and metal thickness, $d_m = 50$ nm. Then, these samples were incubated in 1 mM of 1-hexadecanethiol (in ethanol) for 48–96 hrs for the alkanethiol molecules to form a well ordered monolayer over the nanoparticles. The fuctionalization with 1-hexadecanethiol prevents the aggregation of nanoparticles and makes them stabilized in solution. The AFM of the Ag nanoparticles coated with a SAM of 1-hexadecanethiol on glass substrate is displayed in Figure 5A, image 1. The LSPR spectrum of the SAM-coated Ag nanoparticles in N_2 is shown in Figure 5B, Spectrum 1, with an extinction maximum at 650 nm. After the modification using SAMs, the samples were rinsed thoroughly in ethanol to remove excess 1-hexadecanethiol. Sonication in neat ethanol was then used to lift the nanoparticles off the substrates. The resultant solution was filtered with 400 nm

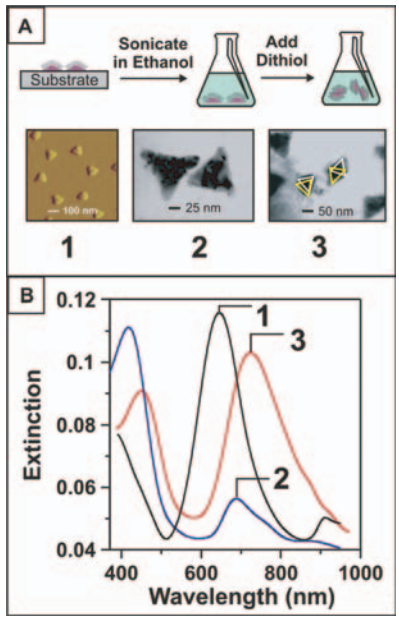

Fig. 5. (A) Schematic illustration of the fabrication of released Ag nanoparticles coated with monolayer of 1-hexadecanethiol and corresponding AFM or TEM images of the nanoparticles at each step. Image 1 is the AFM image of Ag nanotriangles confined on a glass surface; Image 2, the TEM image of released Ag nanotriangles in solution; and image 3, the TEM image of dithiol-linked Ag nanoparticle dimers in solution. (B) Corresponding extinction spectra of Ag nanoparticles. Spectrum 1 is for Ag nanoparticles on glass substrate in N_2; Spectrum 2, for released nanoparticles in ethanol; and Spectrum 3, for nanoparticle dimers in ethanol.

filters (GEOsmonics, Inc., Minnetonka, MN) to remove large particles arising from defects in the nanosphere mask. The morphology of these nanoparticles is revealed by TEM (Fig. 5A image 2). The corresponding UV-vis spectrum of the solution-phase nanoparticles is shown in Figure 5B Spectrum 2, with an intense peak at 418 nm and a weak broad peak centered at 682 nm, which dramatically changed in comparison to Spectrum 1.

Notice that all sides of the released nanoparticles, expect for their bases, are coated with SAM of 1-hexadecanethiol during the stabilization and releasing process, 1,6-hexanedithiol was added to the nanoparticle solution to asymmetrically functionalize the nanoparticles. The formation and geometry of nanoparticle dimers are proved by TEM (Fig. 5A, image 3). Upon the addition of the linking molecules, the nanoparticles are linked to form dimers and an immediate change in the UV-vis spectrum of the nanoparticle solution is observed and shown in Figure 5B, Spectrum 3. In contrast to Spectrum 2, the extinction maximum located at 417.9 nm shifts to 430.5 nm and decreases in intensity while the local maximum located at 682.1 shifts to 705.2 nm and increases in intensity.

To understand the spectral changes described above, Mie theory (data not shown) and DDA method are used to model the extinction spectra of the released nanoparticle monomer and dimer. All calculations are done in ethanol

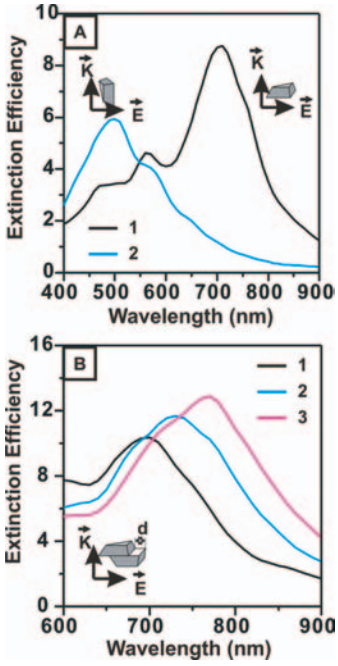

Fig. 6. DDA modeling of the extinction spectra of truncated tetrahedral Ag nanoparticles with a SAM of 1-hexadecanethiol in an ethanol environment. (A) Calculated spectra of single nanoparticle. Spectrum 1 arises from the in-plane porlarization; Spectrum 2 from the out-of-plane polarization. (B) Calculated spectra of a pair of linked Ag nanoparticles. The degree of non-overlap between the two bases of the Ag nanotriangles (denoted as *d*) is (A) 15 nm, (B) 20 nm, and (C) 25 nm, respectively.

environment. When sonicated off the substrates, some of the nanoparticles broke into small fragments. From Mie theory modeling, these fragments are assumed to be spherical and they have an extinction maximum at ~400 nm. The DDA method is utilized to model the extinction spectrum of a single hexadecanethiol-modified Ag truncated tetrahedron in ethanol. As shown in Figure 6A, the in-plane polarization (black line) has a maximum that is located at ~710 nm which corresponds to the "red" peak in Figure 6A, Spectrum 2. The out-of-plane polarization (blue line) has a local extinction maximum located at ~500 nm, which combined with the small fragment absorption may be the cause of the "blue" peak in Figure 5A, Spectrum 2. The small discrepancy between experimental results and modeling arises from that the geometry of nanostructures used in modeling is slightly different from the NSL produced nanotriangles.

From the TEM image in Figure 5B, image 2, the nanoparticles have been asymmetrically linked to form dimers with different degree of overlap between two particles. The in-plane polarization extinction spectra have been calculated using the DDA method for dimers that have varying overlap between the two nanoparticles. It can be seen in Figure 6B that the extinction maxima are in the range $\sim 725 \pm 30$ nm for the overlapped distance, *d* (schematically illustrated in the inset to Fig. 6B) within a range of 15–25 nm. This agrees well with the experimental extinction maximum of the nanoparticle dimers located at 705 nm in Figure 6A, Spectrum 3.

In conclusion, this work has demonstrated a general NSL method which can be used to fabricate uniform solution-phase triangular Ag nanoparticles with precisely-controlled geometry. In addition, this technique allows the asymmetrical assembling of Ag nanoparticle dimers. The optical properties of the released nanoparticles have been monitored with UV-Visible spectroscopy and modeled by Mie theory and the DDA method. Upon the addition of linking agents, the extinction spectrum of the released nanoparticles changes drastically caused by the formation of dimers. This property opens up the probability to use these nanoparticles to detect small biological targets.

3. NANOPORES FABRICATED BY NSL AND RIE: VARIANT OF NSL AND AR NSL

The combination of NSL with RIE is capable of fabricating size-tunable triangular nanopores in single crystal silicon (111) substrates. RIE is a natural choice to use with NSL masks because of its parallel and highly anisotropic properties. Specifically, it has been shown that this combination approach is ideal for the creation of nanopores with the following unique properties:

(1) extremely uniform nanopores (in-plane widths = 44–404 nm);
(2) controlled nanopore depth (25–250 nm);
(3) controlled, uniform nanopore shapes; and
(4) high area density (~10^{10} pores cm^{-2}).

Figure 7 schematically depicts the procedure of the fabrication of nanopores. Well-ordered monolayer nanosphere masks are fabricated on Si(111) by NSL. The samples are then placed in a RIE chamber and etched with a CF_4 plasma. When the reactive plasma bombards the polystyrene nanospheres, the hydrocarbons are fluorinated and remain intact, however, interaction between the reactive CF_4 plasma and the Si(111) substrate produces volatile SiF_4, thus etching the exposed Si(111) surface area. The resulting nanostructure is a well ordered periodic array of

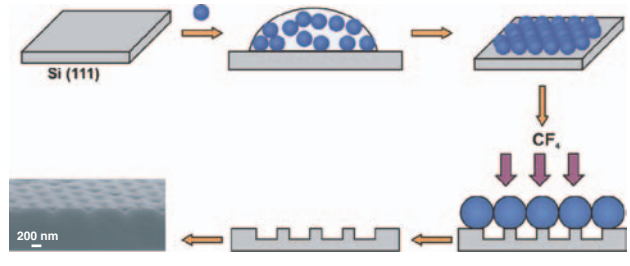

Fig. 7. Schematic representation of nanopore fabrication by NSL and RIE. Reproduced with permission from [40], A. V. Whitney et al., *Nano Lett.* 4, 1507 (**2004**). © 2004, American Chemical Society.

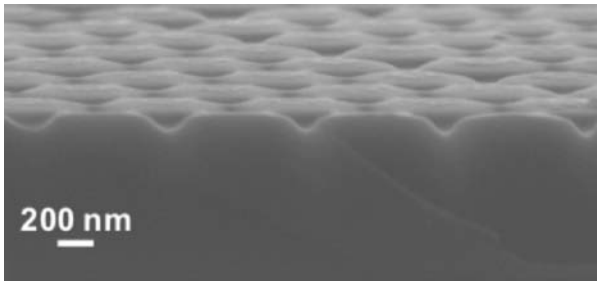

Fig. 8. SEM image of a cross-section of nanopores fabricated with a 720 nm diameter nanosphere etch mask with an etch time = 4 min. Reproduced with permission from [40], A. V. Whitney et al., *Nano Lett.* 4, 1507 (**2004**). © 2004, American Chemical Society.

triangular cross-section nanopores. A cross-sectional SEM image of a typical nanopore array is shown in Figure 8.

The RIE variant of AR NSL yields a further reduction in nanopore in-plane widths.[46] The fabrication of nanopores by AR NSL and RIE begins with a self-assembled NSL etch mask. The sample substrate and etch mask are then mounted on a machined aluminum block in order to obtain the desired angle, (Θ). The sample is then placed in the RIE chamber and etched as described above. The geometry of the nanopores was predicted using the symbolic mathematics program.[46] The worksheet was used to determine the projection of the nanosphere mask onto a substrate for a specified Θ and azimuthal angle (Φ). The generated graphical representations of the nanopore shapes were compared to the fabricated nanopore geometries observed with SEM. While Θ can be easily controlled by etching geometry, imperfections in the nanosphere mask make it difficult to control Φ resulting in a single sample containing several nanopore geometries. Determining Φ was done by choosing a value that gave the best overall shape fit for the experimentally controlled Θ values.

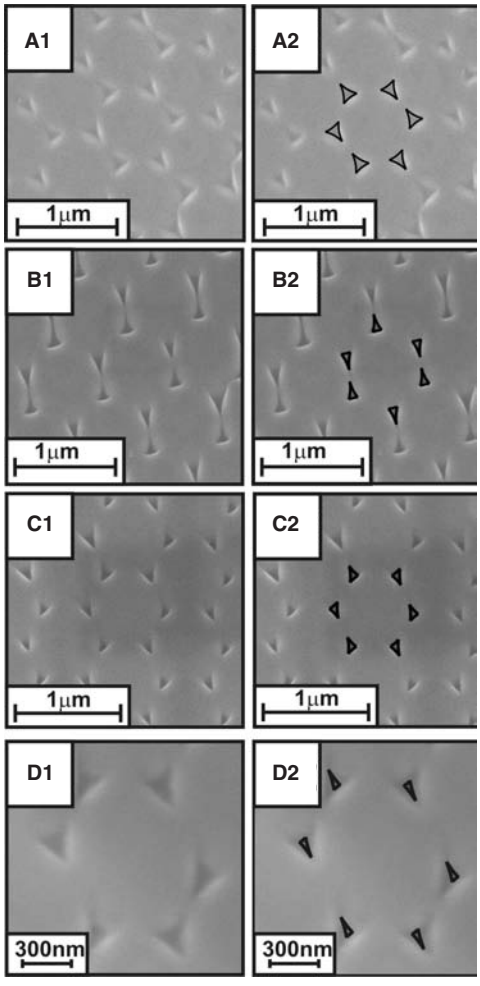

Fig. 9. SEM images of nanopores fabricated using AR NSL and images with simulated superimposed geometries, respectively. (A1, A2) $\Theta = 20°$, $\Phi = 5°$; (B1, B2) $\Theta = 30°$, $\Phi = 1°$; (C1, C2) $\Theta = 30°$, $\Phi = 24°$; and (D1, D2) $\Theta = 40°$, $\Phi = 10°$. All nanopores were made with 720 nm etch masks on Si(111). Etch time = 2 min. Reproduced with permission from [40], A. V. Whitney et al., *Nano Lett.* 4, 1507 (**2004**). © 2004, American Chemical Society.

Figure 9 depicts SEM images of the resulting nanopores (3A-1, 3B-1, 3C-1, and 3D-1) paired with their theoretically predicted geometric representations (3A-2, 3B-2, 3C-2, and 3D-2). The geometrically predicted representations of the pore apertures corresponded well. Furthermore, the in-plane widths ranged from 93 nm to 177 nm, demonstrating a three-fold decrease in the dimensions of the nanopore aperture.

The sub-100 nm nanopores described above have potential application in catalysis, optics, magnetics, sensing, molecular separation, molecular dynamics, and single molecule detection. Additionally, because of their size uniformity, these nanopores provide the ideal template to fabricate a variety of optical and magnetic nanoparticles.

4. ELECTROCHEMICAL TUNING OF NSL-PRODUCED NANOPARTICLES

This section describes our recent efforts to broaden the scope of NSL by fabricating truncated tetrahedral Ag nanoparticles on indium tin oxide (ITO) coated glass electrode surfaces. Well-ordered nanoparticle arrays on conducting transparent surfaces permit the simultaneous study of both optical and electrochemical measurements. Specifically, these new plasmonic materials enable the study of the effect of the electrochemical potential on the LSPR of Ag nanoparticles.

Recently it has been demonstrated that the LSPR λ_{max} of chemically reduced silver nanoparticles shifts ~20–40 nm towards shorter wavelengths due to the increase in negative surface charge density on an ITO electrode surface with the application of potentials from 0 to −2 V (versus Ag/AgCl).[96,97] Poly(acrylic acid)[96,97] or aminobutylsiloxane[98] has been utilized to immobilize noble metal colloids onto ITO surfaces, which make it difficult to fabricate a well-ordered and repeatable surface motif, and therefore, to achieve controllable LSPR spectra.[99] Moreover, when anodic potentials were applied to silver colloid modified electrode surfaces, a total dissolution of colloids was

observed.[100] In contrast, NSL produced nanoparticle arrays have controlled shape, size, and interparticle spacing, and are extremely stable to positive surface charge density on an ITO surface electrode. This makes NSL produced arrays a prime candidate for the use in the systematic study of electrochemical modification of nanoparticles.

This section addresses two goals:

(1) to develop a simple electrochemical method to modify the structure of NSL-fabricated silver nanoparticles and monitor these structure changes by *in situ* LSPR; and

(2) to explore the electrochemical properties of Ag nanoparticles and other nanoscale materials.

Ag nanoparticle arrays on ITO were placed in aqueous 0.1 M $NaClO_4$ and a single cyclic voltammetric sweep was performed to evaluate their oxidation potential (Fig. 10A, solid line). A parallel measurement (Fig. 10A, dashed line) was carried out on Ag film/ITO electrode ($d_m = 50 \pm 5$ nm). The oxidation of silver on a Ag film/ITO surface occurs around $\sim +287$ mV, which is in agreement with previous results.[101] In comparison, the cyclic voltammogram of the Ag nanoparticle arrays on an ITO electrode shows a broader peak, with a less positive onset potential. Clearly, some portion of the Ag nanoparticle arrays oxidize more easily than the bulk Ag film. Assuming that the surface free energy is the same for metal nanoparticles and bulk metal surfaces, then the Kelvin equation predicts that metal nanoparticles will exhibit a standard electrode potential, E^0, that is shifted to more negative potentials than the E^0 of the bulk metal.[102–104] A negative shift in E^0 of small nanoparticles means that smaller metal nanoparticles are more easily oxidized than the bulk material.[102, 105–107]

A potential step from +200 to +400 mV was used in a chronocoulometry experiment to measure the charge required to oxidize the silver nanoparticles confined on

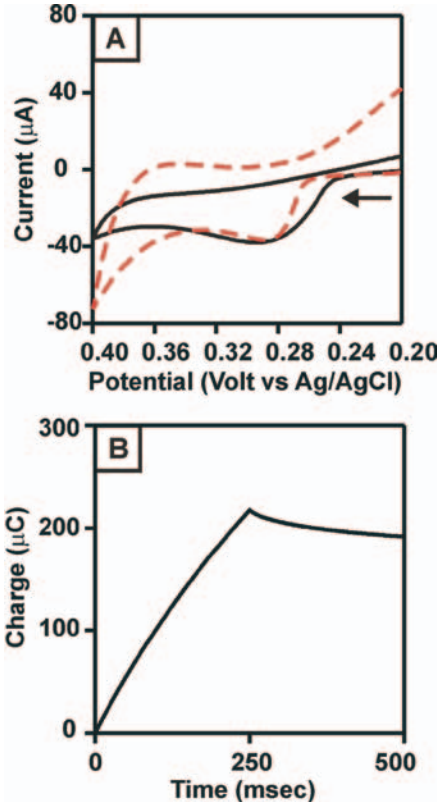

Fig. 10. (A) Single scan cyclic voltammograms of Ag film/ITO (dashed line, $d_m = 50 \pm 5$ nm) and Ag nanoparticle arrays on an ITO electrode (solid line) in 0.1 M $NaClO_4$ aqueous solution. Scan rate = 0.1 V/s. The arrow shows the initial scan direction. (B) Chronocoulometry plot of charge versus time for Ag nanoparticles on an ITO surface (0.64 cm^2) during the oxidation of Ag. Initial potential is 0.20 V, and final potential, 0.40 V. Pulse width = 250 msec. $D = 590$ nm, $d_m = 67$ nm. Reproduced with permission from [43], X. Zhang et al., *Nano Lett.* 5, 1503 (**2005**). © 2005, American Chemical Society.

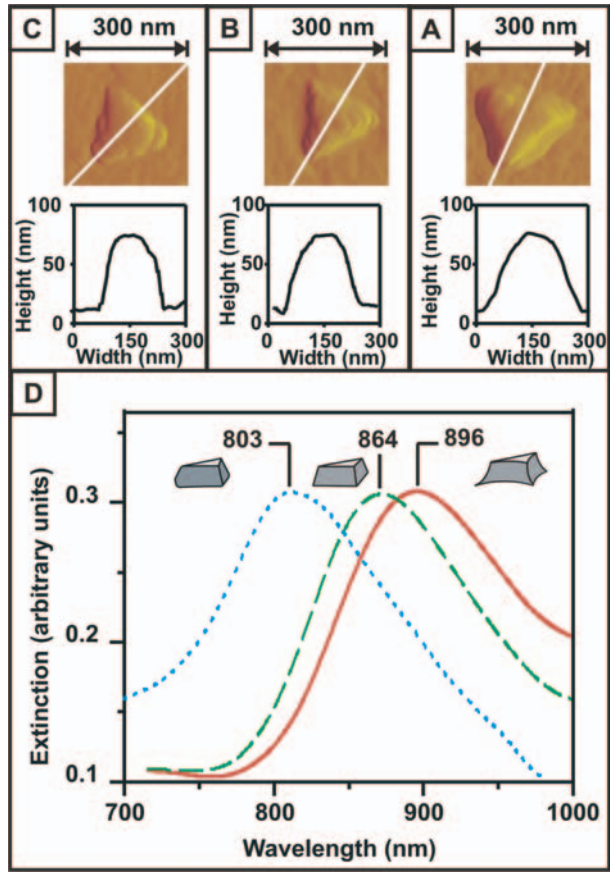

Fig. 11. LSPR spectra and AFM images of Ag nanoparticles on ITO. $D = 590$ nm, $d_m = 68$ nm. (A) LSPR λ_{max} of the Ag nanoparticles shifts towards shorter wavelengths after chronocoulometry measurements. (B) AFM image before any electrochemical measurements. Average Ag nanoparticle out-of-plane height = 68 ± 2 nm and in-plane width = 231 ± 16 nm. LSPR λ_{max} is 896 nm (solid line). (C) AFM image after one chronocoulometry measurement. Average Ag nanoparticle height = 68 ± 3 nm and width = 201 ± 12 nm. LSPR λ_{max} is 864 nm (dashed line). (D) AFM after two chronocoulometry measurements. Average Ag nanoparticle height = 68 ± 3 nm and width = 178 ± 10 nm. LSPR λ_{max} is 803 nm (dotted line). All LSPR spectra were collected in a N_2 environment. Reproduced with permission from [43], X. Zhang et al., *Nano Lett.* 5, 1503 (**2005**). © 2005, American Chemical Society.

the ITO surface (Fig. 10B). Controllable tuning of the Ag nanoparticle structure can be achieved by changing the electrochemical oxidation charge over the range of 10–1000 μC. In addition, the SEM studies reveal the continued presence of well-ordered Ag nanoparticle arrays after repeated electrochemical oxidations, demonstrating high stability of Ag nanoparticle arrays on ITO.[43]

A systematic study to relate electrochemically oxidized nanoparticle structures and optical properties was carried out by combining LSPR spectroscopy and AFM. Figure 11 shows LSPR spectra and the corresponding AFM images of a Ag nanoparticle array on an ITO electrode during a succession of two measurements. The corresponding AFM measurements indicate that the Ag nanoparticle arrays remain constant in height (~68 nm) throughout the two chronocoulometry runs. After the first chronocoulometry measurement (~300 μC/cm^2), the base of the truncated tetrahedral structure decreased from 231 to 201 nm, creating a trigonal prism structure (Fig. 11B). Further electrochemical oxidation (~330 μC/cm^2) removed small amounts of silver from the truncated tetrahedral tips of the nanoparticle, while not changing the nanoparticle's out-of-plane height (Fig. 11C). The order of electrochemical oxidation of the truncated tetrahedral nanoparticles, therefore, can be summarized as the following: Bottom edges first, then top triangular tips, and finally out-of-plane height.

To understand this behavior, we note that Pleith[103] and Makov[108] have previously studied the size-dependent electrochemical behavior of spherical nanoparticles, and they were able to rationalize their results assuming that the surface free energy makes a repulsive contribution to the electrochemical potential which varies as the inverse of the nanosphere radius. In the present context, we would expect that regions of the nanoparticle surface with the smallest radii of curvature should oxidize most readily, so the bottom edges can precede the tips as long as the latter are sufficiently rounded (as seems to be the case from the AFM pictures).

5. THE LOCALIZED SURFACE PLASMON RESONANCE NANOSENSOR: A HIGH RESOLUTION DISTANCE DEPENDENCE STUDY USING ATOMIC LAYER DEPOSITION

The localized surface plasmon resonance (LSPR) wavelength shift response, $\Delta\lambda_{max}$, of Ag nanoparticles fabricated by NSL has been used to develop a new class of nanoscale optical biosensors. The LSPR wavelength shift response of these sensors can be understood, on the most straightforward level, using a model of the refractive-index response of propagating surface plasmons on a planar noble metal surface:

$$\Delta\lambda_{max} = m\Delta n\left[1 - \exp\left(\frac{-2d}{l_d}\right)\right] \quad (1)$$

where $\Delta\lambda_{max}$ is the wavelength shift, m is the refractive-index sensitivity, Δn is the change in refractive index induced by an adsorbate, d is the effective adsorbate layer thickness, and l_d is the characteristic electromagnetic field decay length. While this oversimplified model does not quantitatively capture all aspects of the LSPR nanosensor response, it does provide some guidance for sensor optimization. Particularly, Eq. (1) demonstrates the distance dependence as described by the of the electromagnetic field decay length, l_d.

Haes and co-workers studied the long range distance dependence of the LSPR nanosensor using self-assembled monolayers (SAMs) of 11-mercaptoundecanoic acid (11-MUD) and Cu^{2+} ions fabricated on noble metal nanoparticles with various sizes, shapes, and compositions.[109] The spatial resolution of this experiment was limited to the thickness of the 11-MUD/Cu^{2+} monolayer (~1.6 nm). Several long-range characteristics were found including:

(1) the LSPR shift versus SAM thickness is nonlinear;

(2) Ag nanoparticles are more sensitive than Au nanoparticles;

(3) nanotriangles have larger sensing volumes than nanohemispheoids;

(4) increasing nanoparticle in-plane widths results in larger sensing volumes; and

(5) decreasing nanoparticle out-of-plane height results in larger sensing volumes.[109]

Similarly, the short range distance dependence (0–3 nm) of the LSPR nanosensor has been studied using alkanethiol, $CH_3(CH_2)_xSH$ (x = 2–11, 13–15, and 17), monolayers.[109] It was found that Eq. (1) does a remarkably good job of accounting for the short range LSPR response if one assumes a value l_d = 5–6 nm. In addition, the dependence of $\Delta\lambda_{max}$ on the chain length of the alkanethiol monolayer was found to be linear, with a large slope of 3.1–3.3 nm per CH_2 unit.

Even though important information was obtained from these previous long and short range distance dependence studies, it was expected that new information could be obtained if it were possible to deposit single layers of a material with thicknesses of ~1 Å.[109] Atomic Layer Deposition (ALD) is a fabrication method that produces highly uniform and controlled thin films. Precursor gases are alternately pulsed through the reactor and purged away, resulting in a self-limiting growth process that constructs a film of one monolayer at a time.[110] Highly uniform monolayers of Al_2O_3 can be deposited with ~1 Å thickness resolution and a refractive index of 1.57.[111] Depositing Al_2O_3 multilayers onto the noble metal nanosensor allows the short range distance dependence of the LSPR nanosensor to be probed with a 10 times better spatial resolution than previous work.[112]

Al_2O_3 films were fabricated on the Ag nanoparticles by ALD. The reactor utilized in these experiments is similar

to previous publications. TMA and deionized H_2O vapors were alternately pulsed through the reaction chamber utilizing N_2 as the carrier gas at a mass flow rate of 360 sccm and a pressure of 1 Torr using a growth temperature of 50 °C. Al_2O_3 ALD proceeds on a hydroxylated surface according to Scheme 1.[113]

Scheme. 1.

$$\text{(A) } \text{Al–OH}^* + \text{Al(CH}_3)_3 \rightarrow \text{Al–O–Al(CH}_3)_2^* + \text{CH}_4$$

$$\text{(B) } \text{Al–CH}_3^* + \text{H}_2\text{O} \rightarrow \text{Al–OH}^* + \text{CH}_4$$

The asterisks (∗) signify the surface species. One complete AB cycle is 42 s:

(1) TMA reactant exposure time = 1 s,
(2) N_2 purge following TMA exposure time = 10 s,
(3) H_2O reactant exposure time = 1 s,
(4) N_2 purge following H_2O exposure time = 30 s.

Long purge times are necessary at low temperatures to prevent chemical vapor deposition (CVD) of Al_2O_3.

Figure 12 presents SEM images of bare Ag nanoparticles (Fig. 12A) and Ag nanoparticles coated by Al_2O_3 ALD using 100 (Fig. 12B), 200 (Fig. 12C), 400 (Fig. 12D), and 600 (Fig. 12E) AB cycles. Figure 12F depicts a plot of the nanoparticle in-plane width versus AB cycles determined from the SEM images and yields a growth rate of 0.9 Å/cycle.

Figure 13A depicts LSPR λ_{max} extinction spectra and plots triangular Ag nanoparticles with an in-plane width (a) of 90 nm and out-of-plane height (b) of 40 nm. The UV-Vis spectra for Ag nanoparticles with 0–450 cycles of TMA and water is presented in Figure 13A. As subsequent ALD Al_2O_3 layers are completed, the LSPR λ_{max} position red shifts, which is consistent with previous work.[112] Importantly, because Al_2O_3 ALD can be performed one monolayer at a time, monolayer sensing is possible. For nanoparticles with $a = 90$ nm and $b = 40$ nm a 5 nm LSPR λ_{max} shift is observed with the addition of 2 Å of Al_2O_3. ALD of Al_2O_3 allows for the fabrication of Angstrom thick monolayers which gives this work a 10x increase in the spatial resolution compared to previous work.[109]

Figures 13B and 13C depict LSPR extinction spectra and plots of LSPR λ_{max} shift versus Al_2O_3 film thickness for triangular nanoparticles with in-plane widths of 90 nm and out-of-plane heights of 30 nm (1), 40 nm (2), 51 nm (3). Figure 13B shows a plot of LSPR λ_{max} shift versus Al_2O_3 film thickness for 0–600 AB cycles. At short distances from the nanoparticle surface, the LSPR λ_{max} shift follows a steep linear slope, but as the distance from the nanoparticle increases, the curve bends over, and eventually levels off once the nanoparticle has reached its saturation point. As the nanoparticle height decreases and the in-plane width remains constant, the LSPR λ_{max} shift increases. Figure 13C depicts a plot of LSPR λ_{max} shift versus Al_2O_3 film thickness for 0–20 AB cycles. After each cycle a LSPR extinction spectrum was collected which presents a highly detailed view of the short range distance dependence of the LSPR nanosensor. The SAMs used previously were ∼1.5 nm thick and this limited the information obtainable about the short range distance dependence of the LSPR nanosensor.[109] Because Al_2O_3 ALD layers are ∼1 Å this is the first time that an extremely detailed picture of the short range distance dependence of the LSPR nanosensor has been presented. In fact, the results in this work show that at short distances from the nanoparticle surface, the LSPR λ_{max} shift versus layer thickness follows a steep linear trend compared with

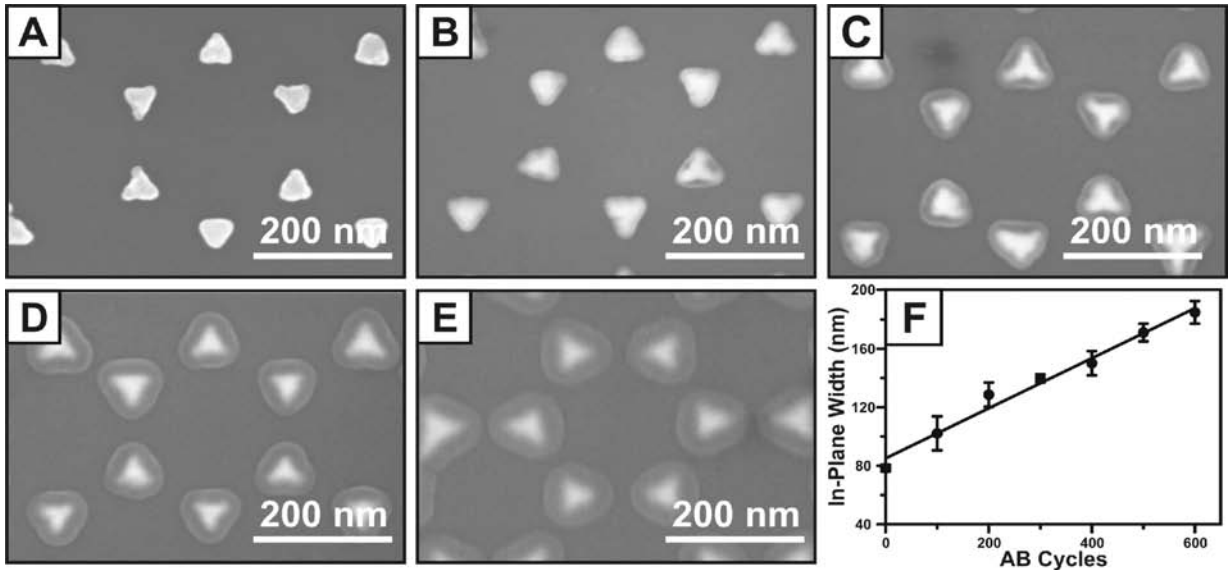

Fig. 12. SEM images of (A) bare Ag nanoparticles ($a = 90$ nm, $b = 51$ nm) and Ag nanoparticles following (B) 100, (C) 200, (D) 400, and (E) 600 AB cycles of TMA/H_2O. (F) Plot of in-plane Ag triangle width versus AB cycles determined from SEM images. Reproduced with permission from [92], A. V. Whitney et al., *J. Phys. Chem. B* 109, 20522 **(2005)**. © 2005, American Chemical Society.

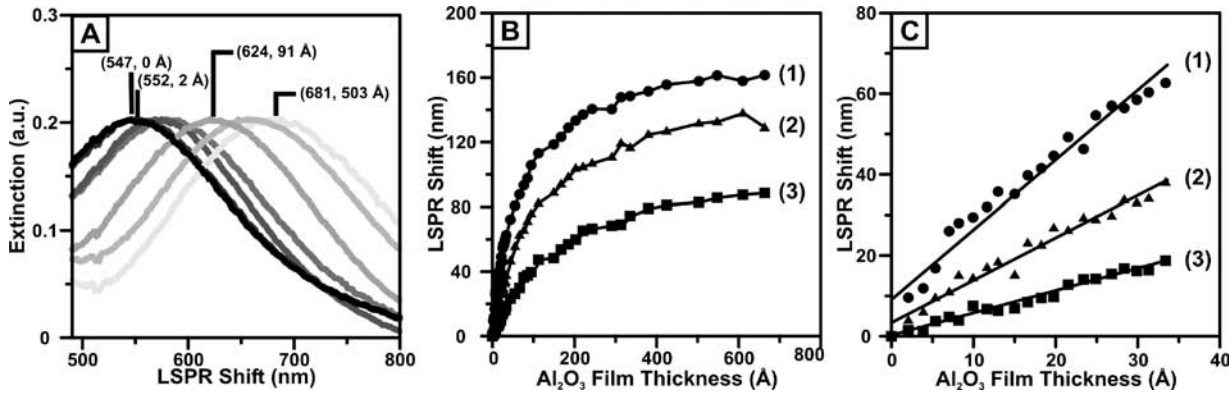

Fig. 13. (A) LSPR spectroscopy of Ag nanoparticles ($a = 90$ nm, $b = 40$ nm) for 0–450 AB cycles of TMA and water. (B) Plot of LSPR shift versus Al_2O_3 film thickness. Out-of plane height dependence on the long and short range distance dependence for Ag triangular nanoparticles $a = 90$ nm and $b = (1)$ 30 nm, (2) 40 nm, and (3) 51 nm. Data presented for 0–600 AB cycles of TMA and water. (C) Plot of LSPR shift versus Al_2O_3 film thickness. Out-of-plane height dependence of the short range distance dependence for the Ag triangular nanoparticles $a = 90$ nm and $b = (1)$ 30 nm, (2) 40 nm, and (3) 51 nm. Data presented for 0–20 AB cycles of TMA and water. Linear regression was used to fit the data to lines described by the following equations: $y = 1.7x + 9.1$; $R^2 = 0.9602$ (1), $1.0x + 3.5$; $R^2 = 0.9689$ (2), and $y = 0.5x + 0.1$; $R^2 = 0.9744$ (3). Reproduced with permission from [92], A. V. Whitney et al., *J. Phys. Chem. B* 109, 20522 **(2005)**. © 2005, American Chemical Society.

the moderate slope at larger distance from the nanoparticle surface. Nanoparticles with fixed in-plane widths and decreasing out-of-plane heights yield larger sensing volumes (Figs. 13C-1) as has been observed at larger distances from the nanoparticle surface.[112]

Using the DDA method,[80, 81, 114, 115] we modeled the LSPR λ_{max} shift measurements for silver particles coated with multilayers of Al_2O_3. In this method, the particle and Al_2O_3 coating are represented using a cubic grid of polarizable elements, with the polarizability of each element determined by the local dielectric constant. The particles are represented as a truncated tetrahedron with dimensions taken to match the experimental results. The grid size in these calculations is 2 nm and the wave vector is taken perpendicular to the bottom surfaces of the truncated tetrahedron or hemispheroid. The refractive index of silver is taken from Hunter and Lynch[116] and that for the adsorbate Al_2O_3 is taken to be 1.57 from the experimental data. The resonance wavelength of the truncated tetrahedron shaped silver particles was calculated with the layer thickness of the Al_2O_3 taken to be the grid size, 2 nm. This is not same as the layer thickness of Al_2O_3, however, the dependence of the LSPR λ_{max} shifts on the layer thickness are not sensitive to this difference for layers that are more than around 5 nm thick. (Fig. 14). Figure 14 shows excellent agreement between the calculated (1) and experimental (2) results for the truncated tetrahedral shape. These results are similar to what has been obtained in previous work involving the long range dependence of the LSPR λ_{max} shifts using SAMs of $CH_3(CH_2)_xSH$ molecules, but here the index of refraction of the Al_2O_3 is known accurately, whereas with the SAM it could only be estimated.[112]

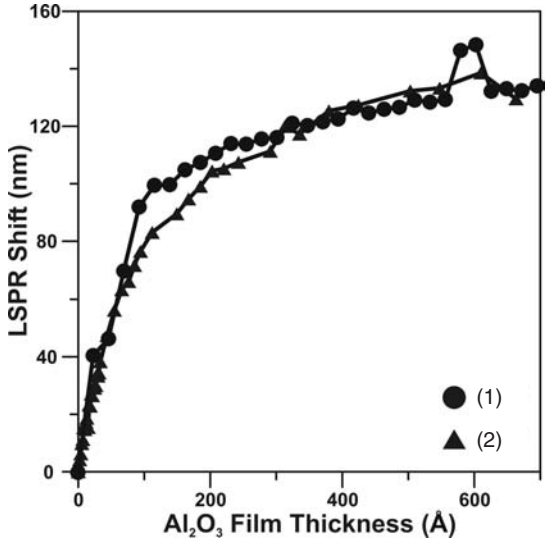

Fig. 14. Plot of calculated (1) and experimental (2) results of LSPR shift versus Al_2O_3 film thickness for bare tetrahedral particles with $a = 90$ nm, $b = 40$ nm. Reproduced with permission from [92], A. V. Whitney et al., *J. Phys. Chem. B* 109, 20522 **(2005)**. © 2005, American Chemical Society.

6. CONCLUSION

We have highlighted representative research accomplishments in the NSL-derived fabrication of silver nanoparticles in solution and on surfaces and their electrochemical and optical properties. This work shows promise for the applications such as point-of-care diagnostics, environmental monitoring, proteomics, drug discovery, and fundamental biological research.

Acknowledgments: The authors gratefully acknowledge support from the National Science Foundation (EEC-0118025, DMR-0076-097, CHE-0414554), the Air Force Office of Scientific Research MURI program (F49620-02-1-0381), by the ARO (Grant DAAG55-97-1-0133), and Chemical Sciences, Geosciences, and Biosciences

Division, Office of Basic Energy Sciences, Office of Science, U.S. Department of Energy (DE-FG02-03ER15457) at the Northwestern University Institute for Environmental Catalysis. Any opinions, findings, and conclusions or recommendations expressed in this paper are those of the authors and do not necessarily reflect those of the National Science Foundation.

References and Notes

1. K. Kempa, B. Kimball, J. Rybczynski, Z. P. Huang, P. F. Wu, D. Steeves, M. Sennett, M. Giersig, D. V. G. L. N. Rao, D. L. Carnahan, D. Z. Wang, J. Y. Lao, W. Z. Li, and Z. F. Ren, *Nano Lett.* 3, 13 **(2003)**.
2. A. J. Haes and R. P. Van Duyne, *J. Am. Chem. Soc.* 124, 10596 **(2002)**.
3. A. D. Mcfarland and R. P. Van Duyne, *Nano Lett.* 3, 1057 **(2003)**.
4. C. L. Haynes and R. P. Van Duyne, *Nano Lett.* 3, 939 **(2003)**.
5. H. D. Tong, H. V. Jansen, V. J. Gadgil, C. G. Bostan, E. Berenschot, C. J. M. Van Rijn, and M. Elwenspoek, *Nano Lett.* 4, 283 **(2004)**.
6. J. Han and H. G. Craighead, *Science* 288, 1026 **(2000)**.
7. R. Gasparac, D. T. Mitchell, and C. R. Martin, *Electrochimica Acta* 49, 847 **(2004)**.
8. S. Howorka, S. Cheley, and H. Bayley, *Nat. Biotechnol.* 19, 636 **(2001)**.
9. K. Landskron, B. D. Hatton, D. D. Perovic, and G. A. Ozin, *Science* 302, 266 **(2003)**.
10. Y. Xia and N. J. Halas, *MRS Bull.* 30, 338 **(2005)**.
11. B. Wiley, Y. G. Sun, B. Mayers, and Y. N. Xia, *Chem.—Eurp. J.* 11, 454 **(2005)**.
12. G. Frens, *Nat.-Phys. Sci.* 241, 20 **(1973)**.
13. R. C. Jin, Y. W. Cao, C. A. Mirkin, K. L. Kelly, G. C. Schatz, and J. G. Zheng, *Science* 294, 1901 **(2001)**.
14. R. Jin, Y. C. Cao, E. Hao, G. S. Metraux, G. C. Schatz, and C. A. Mirkin, *Nature* 425, 487 **(2003)**.
15. J. H. Song, F. Kim, D. Kim, and P. D. Yang, *Chem.—Eurp. J.* 11, 910 **(2005)**.
16. F. Kim, J. H. Song, and P. D. Yang, *J. Am. Chem. Soc.* 124, 14316 **(2002)**.
17. Y. G. Sun and Y. N. Xia, *Science* 298, 2176 **(2002)**.
18. C. J. Brumlik and C. R. Martin, *J. Am. Chem. Soc.* 113, 3174 **(1991)**.
19. M. H. Yun, N. V. Myung, R. P. Vasquez, C. S. Lee, E. Menke, and R. M. Penner, *Nano Lett.* 4, 419 **(2004)**.
20. C. R. Martin, *Science* 266, 1961 **(1994)**.
21. M. Wirtz and C. R. Martin, *Adv. Mater.* 15, 455 **(2003)**.
22. C. J. Murphy, T. K. Sau, A. Gole, and C. J. Orendorff, *MRS Bull.* 30, 349 **(2005)**.
23. B. Wiley, Y. Sun, J. Chen, H. Cang, Z.-Y. Li, X. Li, and Y. Xia, *MRS Bull.* 30, 356 **(2005)**.
24. K. Kneipp, A. S. Haka, H. Kneipp, K. Badizadegan, N. Yoshizawa, C. Boone, K. E. Shafer-Peltier, J. T. Motz, R. R. Dasari, and M. S. Feld, *Appl. Spectrosc.* 56, 150 **(2002)**.
25. L. G. Thygesen, K. Jorgensen, B. L. Moller, and S. B. Engelsen, *Appl. Spectrosc.* 58, 212 **(2004)**.
26. O. J. F. Martin, *Microelectron. Eng.* 67–68, 24 **(2003)**.
27. C. L. Haynes, A. D. Mcfarland, L. L. Zhao, R. P. Van Duyne, G. C. Schatz, L. Gunnarsson, J. Prikulis, B. Kasemo, and M. Kall, *J. Phys. Chem. B* 107, 7337 **(2003)**.
28. M. T. Marshall, M. L. Mcdonald, X. Tong, M. Yeadon, and J. M. Gibson, *Rev. Sci. Instrum.* 69, 440 **(1998)**.
29. D. Brambley, B. Martin, and P. D. Prewett, *Adv. Mater. Opt. Electron.* 4, 55 **(1994)**.
30. J. C. Hulteen and R. P. V. Duyne, *J. Vac. Sci. Technol. A* 13, 1553 **(1995)**.
31. U. C. Fischer and H. P. Zingsheim, *J. Vac. Sci. Technol.* 19, 881 **(1981)**.
32. H. W. Deckman and J. H. Dunsmuir, *Appl. Phys. Lett.* 41, 377 **(1982)**.
33. F. Jarai-Szabo, S. Astilean, and Z. Neda, *Chem. Phys. Lett.* 408, 241 **(2005)**.
34. Home page of Interfacial Dynamics Corp. **(2005)**, http://www.idclatex.com
35. S. B. Han, X. Y. Shi, and F. M. Zhou, *Nano Lett.* 2, 435 **(2002)**.
36. S. B. Han, A. L. Briseno, X. Y. Shi, D. A. Mah, and F. M. Zhou, *J. Phys. Chem. B* 106, 6465 **(2002)**.
37. M. D. Malinsky, K. L. Kelly, G. C. Schatz, and R. P. Van Duyne, *J. Phys. Chem. B* 105, 2343 **(2001)**.
38. X. Zhang, M. A. Young, O. Lyandres, and R. P. Van Duyne, *J. Am. Chem. Soc.* 127, 4484 **(2005)**.
39. A. J. Haes, L. Chang, W. L. Klein, and R. P. Van Duyne, *J. Am. Chem. Soc.* 127, 2264 **(2005)**.
40. A. V. Whitney, B. D. Myers, and R. P. V. Duyne, *Nano Lett.* 4, 1507 **(2004)**.
41. D. A. Stuart, C. R. Yonzon, X. Zhang, O. Lyandres, N. C. Shah, M. R. Glucksberg, J. T. Walsh, and R. P. Van Duyne, *Anal. Chem.* 77, 2013 **(2005)**.
42. C. R. Yonzon, C. L. Haynes, X. Zhang, J. T. Walsh, Jr., and R. P. Van Duyne, *Anal. Chem.* 76, 78 **(2004)**.
43. X. Zhang, E. M. Hicks, J. Zhao, G. C. Schatz, and R. P. V. Duyne, *Nano Lett.* 5, 1503 **(2005)**.
44. J. G. C. Veinot, H. Yan, S. M. Smith, J. Cui, Q. L. Huang, and T. J. Marks, *Nano Lett.* 2, 333 **(2002)**.
45. C. L. Haynes and R. P. V. Duyne, *J. Phys. Chem. B* 105, 5599 **(2001)**.
46. C. L. Haynes, A. D. Mcfarland, M. T. Smith, J. C. Hulteen, and R. P. Van Duyne, *J. Phys. Chem. B* 106, 1898 **(2002)**.
47. A. Kosiorek, W. Kandulski, P. Chudzinski, K. Kempa, and M. Giersig, *Nano Lett.* 4, 1359 **(2004)**.
48. A. Kosiorek, W. Kandulski, H. Glaczynska, and M. Giersig, *Small* 1, 439 **(2005)**.
49. J. Rybczynski, U. Ebels, and M. Giersig, *Colloids and Surfaces A: Physicochem. Eng. Aspects* 1 **(2003)**.
50. Z. C. Zhou, X. S. Zhao, and X. T. Zeng, *Surface and Coatings Technol.* 198, 178 **(2005)**.
51. H. A. Bullen and S. J. Garrett, *Nano Lett.* 2, 739 **(2002)**.
52. D. K. Yi and D. Y. Kim, *Chem. Commun.* 982 **(2003)**.
53. Y. Wang, S. B. Han, A. L. Briseno, R. J. G. Sanedrin, and F. M. Zhou, *J. Mater. Chem.* 14, 3488 **(2004)**.
54. A. L. Briseno, S. B. Han, I. E. Rauda, F. M. Zhou, C. S. Toh, E. J. Nemanick, and N. S. Lewis, *Langmuir* 20, 219 **(2004)**.
55. Y. Cai and B. M. Ocko, *Langmuir* 21, 9274 **(2005)**.
56. S. M. Weekes and F. Y. Ogrin, *J. Appl. Phys.* 97, 10J503/1 **(2005)**.
57. S. M. Weekes, F. Y. Ogrin, and W. A. Murray, *Langmuir* 20, 11208 **(2004)**.
58. Z. P. Huang, D. L. Carnahan, J. Rybczynski, M. Giersig, M. Sennett, D. Z. Wang, J. G. Wen, K. Kempa, and Z. F. Ren, *Appl. Phys. Lett.* 82, 460 **(2003)**.
59. K. H. Park, S. Lee, K. H. Koh, R. Lacerda, K. B. K. Teo, and W. I. Milne, *J. Appl. Phys.* 97 **(2005)**.
60. F. Lenzmann, K. Li, A. H. Kitai, and H. D. H. Stover, *Chem. Mater.* 6 **(1994)**.
61. Y. Lu, C. A. Aguilar, and S. Chen, *Drug Discovery Today: Technologies* 2, 97 **(2005)**.
62. C. Haginoya, M. Ishibashi, and K. Koike, *Appl. Phys. Lett.* 71, 2934 **(1997)**.
63. W. A. Murray, S. Astilean, and W. L. Barnes, *Phys. Rev. B* 69 **(2004)**.
64. Y. Lu, S. Theppakuttai, and S. C. Chen, *Appl. Phys. Lett.* 82, 4143 **(2003)**.
65. C. W. Kuo, J. Y. Shiu, Y. H. Cho, and P. Chen, *Adv. Mater.* 15, 1065 **(2003)**.

66. B. J. Y. Tan, C. H. Sow, T. S. Koh, K. C. Chin, A. T. S. Wee, and C. K. Ong, *J. Phys. Chem. B* 109, 11100 **(2005)**.
67. C. W. Kuo, J. Y. Shiu, P. L. Chen, and G. A. Somorjai, *J. Phys. Chem. B* 107, 9950 **(2003)**.
68. C. W. Kuo, J. Y. Shiu, and P. L. Chen, *Chem. Mater.* 15, 2917 **(2003)**.
69. X. Y. Wang, H. Zhong, J. H. Yuan, D. Sheng, X. Ma, J. J. Xu, and H. Y. Chen, *Chem. Lett.* 33, 982 **(2004)**.
70. Y. D. Wang, S. J. Chua, S. Tripathy, M. S. Sander, P. Chen, and C. G. Fonstad, *Appl. Phys. Lett.* 86 **(2005)**.
71. Y. B. Zheng, S. J. Chua, C. H. A. Huan, and Z. L. Miao, *J. Cryst. Growth* 268, 369 **(2004)**.
72. B. Johnsson, S. Lofas, and G. Lindquist, *Anal. Biochem.* 198, 268 **(1991)**.
73. T. R. Jensen, K. L. Kelly, A. Lazarides, and G. C. Schatz, *J. Cluster Sci.* 10, 295 **(1999)**.
74. T. R. Jensen, M. L. Duval, L. Kelly, A. Lazarides, G. C. Schatz, and R. P. Van Duyne, *J. Phys. Chem. B* 103, 9846 **(1999)**.
75. M. D. Malinsky, K. L. Kelly, G. C. Schatz, and R. P. Van Duyne, *J. Am. Chem. Soc.* 123, 1471 **(2001)**.
76. T. R. Jensen, M. D. Malinsky, C. L. Haynes, and R. P. Van Duyne, *J. Phys. Chem. B* 104, 10549 **(2000)**.
77. G. Mie, *Annalen der Physik* 25, 377 **(1908)**.
78. C. F. Bohren and D. R. Huffman, *Absorption and Scattering of Light by Small Particles*, Wiley Interscience, New York **(1983)**.
79. K. L. Kelly, A. A. Lazarides, and G. C. Schatz, *Comp. Sci. Eng.* 3, 67 **(2001)**.
80. B. T. Draine and P. J. Flatau, *J. Opt. Soc. Am. A* 11, 1491 **(1994)**.
81. B. T. Draine and P. J. Flatau, User Guide for the Discrete Dipole Approximation Code DDSCAT. 6.0 **(2003)**, http://arxiv.org/abs/astro
82. L. Novotny, D. W. Pohl, and B. Hecht, *Opt. Lett.* 20, 970 **(1995)**.
83. A. Taflove, *Computational Electrodynamics: The Finite-Difference Time-Domain Method*, Artech House, Boston **(1995)**.
84. P. W. Barber and S. C. Hill, *Light Scattering by Particles: Computational Methods*, World Scientific, Singapore **(1990)**.
85. T. R. Jensen, G. C. Schatz, and R. P. Van Duyne, *J. Phys. Chem. B* 103, 2394 **(1999)**.
86. A. J. Haes, W. P. Hall, L. Chang, W. L. Klein, and R. P. Van Duyne, *Nano Lett.* 4, 1029 **(2004)**.
87. C. R. Yonzon, E. Jeoung, S. L. Zou, G. C. Schatz, M. Mrksich, and R. P. Van Duyne, *J. Am. Chem. Soc.* 126, 12669 **(2004)**.
88. J. C. Riboh, A. J. Haes, A. D. Mcfarland, C. R. Yonzon, and R. P. Van Duyne, *J. Phys. Chem. B* 107, 1772 **(2003)**.
89. C. R. Yonzon, X. Zhang, and R. P. Van Duyne, *Proc. SPIE-Int. Soc. Opt. Eng.* 5224, 78 **(2003)**.
90. A. Ormonde, E. M. Hicks, J. Castillo, and R. P. Van Duyne, *Langmuir* 20, 6927 **(2004)**.
91. A. J. Haes, J. Zhao, S. Zou, G. C. Schatz, and R. P. Van Duyne, *J. Phys. Chem. B* 109, 11158 **(2005)**.
92. A. V. Whitney, J. W. Elam, S. L. Zou, A. V. Zinovev, P. C. Stair, G. C. Schatz, and R. P. Van Duyne, *J. Phys. Chem. B* 109, 20522 **(2005)**.
93. A. S. Dimitrov and K. Nagayama, *Langmuir* 12, 1303 **(1996)**.
94. P. C. Lee and D. Meisel, *J. Phys. Chem.* 86, 3391 **(1982)**.
95. J. C. Hulteen, D. A. Treichel, M. T. Smith, M. L. Duval, T. R. Jensen, and R. P. Van Duyne, *J. Phys. Chem. B* 103, 3854 **(1999)**.
96. Z. Wang and G. Chumanov, *Adv. Mater.* 15, 1285 **(2003)**.
97. R. Chapman and P. Mulvaney, *Chem. Phys. Lett.* 349, 358 **(2001)**.
98. A. Toyota, N. Nakashima, and T. Sagara, *J. Electroanal. Chem.* 565, 335 **(2004)**.
99. L. Gunnarsson, T. Rindzevicius, J. Prikulis, B. Kasemo, M. Kall, S. L. Zou, and G. C. Schatz, *J. Phys. Chem. B* 109, 1079 **(2005)**.
100. T. Ung, M. Giersig, D. Dunstan, and P. Mulvaney, *Langmuir* 13, 1773 **(1997)**.
101. I. O. K'owino, R. Agarwal, and O. A. Sadik, *Langmuir* 19, 4344 **(2003)**.
102. W. J. Plieth, *Surf. Sci.* 156, 530 **(1985)**.
103. W. J. Plieth, *J. Phys. Chem.* 86, 3166 **(1982)**.
104. L. R. Fisher and J. N. Israelachvili, *J. Colloid. Interf. Sci.* 80, 528 **(1981)**.
105. N. K. Chaki, J. Sharma, A. B. Mandle, I. S. Mulla, R. Pasricha, and K. Vijayamohanan, *Phys. Chem. Chem. Phys.* 6, 1304 **(2004)**.
106. P. L. Redmond, A. J. Hallock, and L. E. Brus, *Nano Lett.* 5, 131 **(2005)**.
107. K. H. Ng, H. Liu, and R. M. Penner, *Langmuir* 16, 4016 **(2000)**.
108. G. Makov, A. Nitzan, and L. E. Brus, *J. Chem. Phys.* 88, 5076 **(1988)**.
109. A. J. Haes, S. Zou, G. C. Schatz, and R. P. Van Duyne, *J. Phys. Chem. B* 108, 109 **(2004)**.
110. M. Ritala and M. Leskela, Handbook of Thin Film Materials 1, 103 **(2002)**.
111. A. W. Ott, J. W. Klaus, J. M. Johnson, and S. M. George, *Thin Solid Films* 292, 135 **(1997)**.
112. A. J. Haes, S. Zou, G. C. Schatz, and R. P. Van Duyne, *J. Phys. Chem. B* 108, 109 **(2004)**.
113. J. W. Elam, M. D. Groner, and S. M. George, *Rev. Sci. Instrum.* 73, 2981 **(2002)**.
114. K. L. Kelly, E. Coronado, L. Zhao, and G. C. Schatz, *J. Phys. Chem. B* 107, 668 **(2003)**.
115. S. Zou, L. Zhao, and G. C. Schatz, *Proc. SPIE-Int. Soc. Opt. Eng.* 5221, 174 **(2003)**.
116. D. W. Lynch, W. R. Hunter, and E. D. Palik, Handbook of Optical Constants of Solids, Academic Press, New York **(1985)**.

Received: 8 December 2005. Revised/Accepted: 4 March 2006.